



HAL
open science

Nanoscale Isotopic Dating of Monazite

Denis Fougrouse, Christopher Kirkland, David Saxey, Anne-Magali Seydoux-Guillaume, Matthew Rowles, William Rickard, Steven Reddy

► **To cite this version:**

Denis Fougrouse, Christopher Kirkland, David Saxey, Anne-Magali Seydoux-Guillaume, Matthew Rowles, et al.. Nanoscale Isotopic Dating of Monazite. *Geostandards and Geoanalytical Research*, 2020, 10.1111/ggr.12340 . hal-02996416

HAL Id: hal-02996416

<https://hal.science/hal-02996416>

Submitted on 16 Nov 2020

HAL is a multi-disciplinary open access archive for the deposit and dissemination of scientific research documents, whether they are published or not. The documents may come from teaching and research institutions in France or abroad, or from public or private research centers.

L'archive ouverte pluridisciplinaire **HAL**, est destinée au dépôt et à la diffusion de documents scientifiques de niveau recherche, publiés ou non, émanant des établissements d'enseignement et de recherche français ou étrangers, des laboratoires publics ou privés.

1 Nanoscale isotopic dating of monazite

2 Denis Fougereuse^{1,2}, Christopher Kirkland¹, David Saxey², Anne-Magali Seydoux-
3 Guillaume^{3,4}, Matthew R. Rowles², William D.A. Rickard², Steven M. Reddy¹

4 ¹School of Earth and Planetary Sciences, Curtin University, Perth, Australia

5 ²Geoscience Atom Probe, Advanced Resource Characterisation Facility, John de Laeter Centre,
6 Curtin University, Perth, Australia

7 ³CNRS, Université de Lyon, UCBL, ENSL, LGL-TPE, 69622 Villeurbanne, France.

8 ⁴Univ Lyon, UJM-Saint-Etienne, F-42023 SAINT-ETIENNE, France

9

10 **Abstract**

11 Monazite U-Th-Pb geochronology is widely used for dating geological processes, but current
12 analytical techniques are limited to grains greater than 5 μm in diameter. This limitation
13 precludes the analysis of both micrometre-scale discrete monazite grains and fine textures
14 within monazite crystals that are commonly found. Here, we analyse reference materials by
15 atom probe tomography and develop a protocol for $^{208}\text{Pb}/^{232}\text{Th}$ dating of nanoscale domains
16 of monazite ($0.0007 \mu\text{m}^3$ analytical volume). The results indicates that the $^{208}\text{Pb}^{++}/^{232}\text{ThO}^{++}$ are
17 higher than the true values. Such fractionation can be corrected using a linear regression
18 between $^{208}\text{Pb}^{++}/^{232}\text{ThO}^{++}$ and the $M/\Delta M_{10}$ peak shape parameter, where M is the position of the
19 O_2^+ peak and ΔM_{10} the full-width-tenth-maximum for the same peak. This correction results
20 in 15 to 20 % analytical uncertainty on the corrected $^{208}\text{Pb}/^{232}\text{Th}$ age. Nonetheless, this approach
21 opens the possibility of obtaining $^{208}\text{Pb}/^{232}\text{Th}$ ages with sufficient precision to address
22 geological questions on an unprecedented small scale. To illustrate the approach, atom probe
23 geochronology of a small monazite grain from the contact aureole of the Fanad pluton
24 (Ireland) yielded a $^{208}\text{Pb}/^{232}\text{Th}$ atom probe age of $420 \pm 60 \text{ Ma}$ (2σ) and is consistent with the
25 known metamorphism in the region.

26

27

28

29 1. Introduction

30 The light rare earth element phosphate (LREEPO₄) monazite is used widely to establish the
31 timing of rock formation, metamorphism, hydrothermal alteration, and deformation (Parrish,
32 1990; Janots et al., 2012; Seydoux-Guillaume et al., 2012; Wawrzenitz et al., 2012; Erickson et
33 al., 2015; Laurent et al., 2018). In particular, monazite may dissolve and regrow in entirety or
34 partially during fluid-rock interaction, providing a high-fidelity temporal record of this
35 process (Poitrasson et al., 2000; Janots et al., 2008; Kirkland et al., 2009; Allaz et al., 2013).
36 During crystallisation, monazite may incorporate several 1000s ppm of U and up to 25% Th
37 which will undergo radioactive decay to Pb at a rate appropriate for geological studies
38 (Parrish, 1990). *In situ* radiometric dating of monazite thus can be performed using a number
39 of analytical techniques, including laser ablation inductively coupled plasma mass
40 spectrometry (LA-ICPMS) and secondary ionization mass spectrometry (SIMS). However,
41 each isotopic measurement technique has an associated analytical volume (Fig. 1). The
42 techniques attaining the smallest analytical volume can reach down to ~9 μm³ for NanoSIMS
43 (Yang et al., 2012) and 2.5 μm³ for SIMS depth profiling (Grove and Harrison, 1999). However,
44 such analytical volumes are too large to effectively date micrometre to sub-micrometre
45 monazites and their associated textures. As a result, the geological record contained within
46 small monazites and their fine textural domains is unexplored. Nanoscale analyses of
47 monazites have also revealed 10-20 nm Pb-rich clusters and partial replacement reactions
48 (Seydoux-Guillaume et al., 2003; Grand'Homme et al., 2016). Atom Probe Tomography (APT)
49 is capable of measuring the isotopic compositions of minerals at the nanoscale for volumes
50 <0.0007 μm³, four to six order of magnitude smaller than other high spatial resolution
51 techniques (Reddy et al., 2020). The APT analytical approach has been shown to be important
52 in refining our understanding of other accessory mineral geochronometers including zircon
53 (Valley et al., 2014; Valley et al., 2015; Peterman et al., 2016), Baddeleyite (White et al., 2017),
54 and titanite (Kirkland et al., 2018), but the potential that nanogeochronology has to unlock
55 otherwise untraceable information remains largely unexplored.

56 Previous APT analyses of monazite has revealed heterogeneous nanoscale distribution of Pb
57 that has the potential to be used to trace the geological history of the mineral (Fougerouse et
58 al., 2018; Seydoux-Guillaume et al., 2019). However, ²⁰⁸Pb/²³²Th ages extracted from these

59 analyses were inaccurate. These previous studies systematically overestimated the $^{208}\text{Pb}/^{232}\text{Th}$
60 ratio; however, the reasons for overestimation remained unclear in that work. Nonetheless,
61 the overestimation was hypothesized to result from geological processes leading to
62 unsupported Pb or missing Th from the atom probe mass spectra (Fougerouse et al., 2018). In
63 order to better understand the $^{208}\text{Pb}/^{232}\text{Th}$ age inaccuracy of APT data, and any instrumental
64 effects, we have analysed five monazite reference materials of varying composition and age.

65 **2. Samples**

66 Five monazite reference materials were selected for this study; C-83-32 ($2,685 \pm 2$ Ma; (Corfu,
67 1988; Kirkland et al., 2009)), DIG19 (1928 ± 2 Ma; (Schärer and Deutsch, 1990)), B0109G (1137
68 ± 1 Ma; (Bingen et al., 2008)), Manangotry (555 ± 2 Ma; (Paquette and Tiepolo, 2007; Montel et
69 al., 2018)) and Moacyr (504.3 ± 0.2 Ma; (Seydoux-Guillaume et al., 2002; Fletcher et al., 2010;
70 Gasquet et al., 2010)). We analysed one specimen from C-83-32 (M1), two specimens from
71 B0109G (M2 and M3), one from Moacyr (M4), two from DIG19 (M5 and M6) and three
72 specimens from Manangotry (M7, M8 and M9). The composition of the different reference
73 materials varies from 3.01 to 13.25 wt.% ThO_2 , 0.085 to 0.45 wt.% UO_2 and 0.16 to 0.9 wt.%
74 PbO and summarized in Table 1. The Th/U ratio varies from 10 to 66. When possible the
75 standard was selected to ensure concordance and avoid decoupling of the parent-daughter
76 radioactive pair (Seydoux-Guillaume et al., 2019).

77 Additionally, a sample with unknown age from the Fanad contact metamorphic aureole in
78 Ireland was investigated (specimen M10, M11 and M12; see section 5). The grain size
79 distribution of the monazites in the Fanad sample was measured using a Tescan TIMA
80 automated mineralogy Scanning Electron Microscope (SEM) in bright-phase search mode.
81 The bright-phase mode uses backscattered electron images to calculate the monazite grain
82 size. Operating conditions were set at 25 kV and 6 nA, using a spot size of 50 nm with a
83 working distance of 15 mm. The pixel resolution was 1 μm .

84

85 **3. Method**

86 **3.1. Samples preparation**

87 Needle-shaped atom probe specimens were prepared by the lift-out method from the surface
88 of one inch polished resin mounts using a Tescan Lyra3 Ga⁺ focused ion beam mounted on a
89 scanning electron microscope (FIB-SEM) located in the John de Laeter Centre at Curtin
90 University (Rickard et al., 2020). The ion beam was operated at an accelerating voltage of 30
91 kV during the manufacturing of the atom probe specimens, with a final polishing stage at 2
92 kV to remove any surface layer affected by high-energy Ga ion implantation. The final
93 specimen shape was approximately 50 to 100 nm in diameter at the apex of the needle and
94 approximately 300 nm in diameter at 1 μm depth (Fig. 2). Due to the manual manufacturing
95 of the atom probe specimens, each specimen has a slightly different shape.

96 3.2. Atom probe tomography

97 Atom probe tomography is a technique that provides chemical and isotopic information at
98 sub-nanometre resolution in 3-dimensions (Larson et al., 2013). Atoms are positively ionised
99 and evaporated from the apex of needle-shaped specimens under a high electric field. For
100 non-conductive materials, including most geological minerals, a laser pulse is focussed at the
101 apex of the specimen to trigger the field-induced evaporation of an atom. In ideal cases, atoms
102 are evaporated one at a time. Once evaporated, the ions traverse the ion optics and impact on
103 a position-sensitive detector (detection event) that provides information on the lateral position
104 (X-Y) position of the atoms in the specimen. The sequence of detection events is used to
105 establish the location of each ion along the specimen axis (Z). The identification of ions is
106 determined by their time-of-flight between the laser pulse and the detection event. The time-
107 of-flight of an individual ion is characteristic of its mass and charge state, and the combination
108 of all detected ions form a mass/charge ratio spectrum (Da; Fig. 3). During APT analysis, the
109 voltage (V) evolves proportionally to the tip radius at the specimen apex (R). During APT
110 analysis, the voltage (V) is increased in approximate proportion to the radius at the specimen
111 apex (R) in order to maintain a constant rate of ion detection. This corresponds to an
112 approximately constant electric field (E) required for ion evaporation, following equation (1):

$$113 \quad E = \frac{V}{kR} \quad (\text{eq. 1})$$

114 with a geometrical factor, *k*, assumed to be constant and equal to 3.3 for this study. Commonly,
115 the FIB-prepared specimens are conical in shape with the tip radius increasing during APT

116 analysis. As a result, the voltage increases gradually during acquisition (Fig. 2). The size of an
117 atom probe dataset is typically between a few million and one hundred million ions, but can
118 be larger. The shape of the analysed volume is dependent on the original specimen shape but
119 typically has a diameter of 50 to 150 nm and a length of up to 1 μm .

120 In this study, we have used the Cameca Local Electrode Atom Probe (LEAP 4000X HR)
121 housed within the Geoscience Atom Probe facility at Curtin University. The instrument is
122 equipped with a UV laser ($\lambda = 355 \text{ nm}$) and a curved ion flight path (reflectron) in order to
123 increase the mass resolving power and reduce background noise. For all analyses, the
124 specimens were maintained at 60 K, the detection rate at an average of one detected event
125 per 100 laser pulses and the laser was pulsed at 125 kHz. A total of 19 datasets from five
126 different monazite reference standards are reported in this study (Table 2). The raw data
127 was reconstructed using the IVAS software package from Cameca Instruments, version
128 3.8.2. Corrections to the raw time-of-flight data were made using the default settings for
129 both voltage and flight-path ('bowl') corrections. The O_2^+ peak at 32 Da was selected for the
130 time-of-flight corrections, using a 'next to leading order' fit for the voltage correction, and a
131 maximum of 4 subdivisions in the piece-wise two-dimensional bowl correction (Larson et
132 al., 2013). The software found the same solution (FWHM value) for every range width
133 selection for the O_2^+ peak. The mass-to-charge ratio spectra was calibrated using the O^+ , O_2^+ ,
134 PO_2^+ , PO_3^+ , ThO^{++} and $\text{ThP}_2\text{O}_6^{++}$ peaks.

135 To investigate the role of laser energy on atom probe data, two specimens (M1 - C-83-32; and
136 M2 - B0109G) were analysed over a range of laser energies between 20 and 500 pJ (Table 2).
137 Seven datasets were acquired for each of these specimens (M1-1 to M1-7 and M2-1 to M2-
138 7). Such sequential analyses allows investigation of the effect of specific instrument running
139 parameters and permits the separation of the effects of external variables such as differences
140 in needle shape (Table 2). For M1, the laser energy started at 20 pJ (M1-1) and increased to 50
141 pJ (M1-2), 100 pJ (M1-3), 200 pJ (M1-4), 300 pJ (M1-5), 400 pJ (M1-6) and then decreased to
142 300 pJ (M1-7). For M2, the laser energy increased from 50 pJ (M2-1), then 100 pJ (M2-2), 200
143 pJ (M2-3), 300 pJ (M2-4), 400 pJ (M2-5), 500 pJ (M2-6) and then decreased to 300 pJ (M2-7).
144 Five million atoms were acquired for each dataset with the specimen voltage increasing
145 during each acquisition to compensate for the increasing tip radius of the specimen.

146

147 3.3. Isotopic quantification

148 The quantification procedure for isotopes used in this work differs slightly from that applied
149 in previous studies of monazite (Fougerouse et al., 2018). Due to the variable U content of the
150 selected standards, ^{238}U was not always present above the mass spectrum background, and
151 therefore the $^{208}\text{Pb}/^{232}\text{Th}$ isotopic system was used for this study. The quantification of ^{232}Th
152 was limited to the major Th ionic species ThO^{++} . Due to the interference of $\text{REEP}_5\text{O}_5^{+++}$
153 molecules (from 124.25 Da) on the thermal tail of the ThO^{++} peak (124.02 Da), the full ThO^{++}
154 peak cannot be accurately measured. Instead, a narrow range (0.1 Da) was used to measure
155 the counts under the centre of the peak only (Fig. 3 inset). The same narrow range was used
156 to measure the ^{208}Pb counts using only the $^{208}\text{Pb}^{++}$ peak (103.99 Da). Counts for ThO^{++} and $^{208}\text{Pb}^{++}$
157 were quantified by subtracting the estimated background counts from each peak. The local
158 background level was measured from the counts in a wide 'peak-free' range of 1 Da at ~100
159 Da for $^{208}\text{Pb}^{++}$ and of 2 Da at ~130 Da for ThO^{++} (Fig. S1). These background counts were
160 subsequently normalised to the width of the range used for quantification (0.1 Da).
161 Uncertainties for each background-corrected isotopic species were estimated from counting
162 statistics for each isotope peak and its correction. The isotopic ratio uncertainties are derived
163 from the uncertainty of each species used for calculating the ratio and reported at 95%
164 confidence (2 sigma) (Table 2).

165 The instrumental $^{208}\text{Pb}/^{232}\text{Th}$ fractionation parameter (F) is defined by the percentage
166 departure of the APT measured $^{208}\text{Pb}^{++}/^{232}\text{Th}^{16}\text{O}^{++}$ ratio from the reference material true
167 $^{208}\text{Pb}/^{232}\text{Th}$ ratio, as independently determined, following equation (2):

$$168 \quad F = \left(\frac{(^{208}\text{Pb}/^{232}\text{Th})_{\text{True}}}{(^{208}\text{Pb}^{++}/^{232}\text{ThO}^{++})_{\text{Measured}}} \times 100 \right) - 100 \quad (\text{eq. 2})$$

169 Negative values indicate an overestimation of the $^{208}\text{Pb}/^{232}\text{Th}$ ratio and positive values an
170 underestimation of the ratio. In this study, we have used a half-life of 1.405×10^{10} years for ^{232}Th
171 (Audi et al., 2003).

172 3.4. Peak shape quantification

173 When considering probable causes of inaccuracy in $^{208}\text{Pb}/^{232}\text{Th}$ ratios in APT measurements,
174 one of the major influences is likely to be peak-shape variability. Typical mass peak shapes in
175 APT spectra are asymmetric, with an extended tail at the high-mass end due to slow cooling
176 of the specimen tip following the laser pulse. However, the precise shape can vary between
177 acquisitions, depending on materials property and specimen shape, and may also vary
178 between mass peaks within a single dataset, particularly between different
179 elemental/molecular ions and charge states.

180 To completely correct for the full array of influences on quantification due to peak shape
181 variations is a complex problem. However, a robust and quantifiable measure of 'peak shape'
182 can be sought that may provide sufficient quantification of peak shape effects to be useful in
183 correcting any resulting fractionation. In this work, the mass resolving power, measured as
184 the width at one-tenth of maximum peak height ($M/\Delta M_{10}$) was selected as a metric for
185 quantifying the peak shape. In this expression, M is the position of the maximum peak
186 intensity and ΔM_{10} the full-width at tenth-maximum.

187 A method was developed to quantify $M/\Delta M_{10}$, as a proxy for the peak shape. The detailed
188 peak shape quantification is given in the supplementary material. A model curve to a selected
189 peak was fitted using the software package Topas (version 5) (Coelho, 2018). The largest peak
190 in the monazite spectra (O_2^+ ; Fig. 3) was selected in order to increase the signal to noise ratio
191 and maximise counting statistics. Data was imported into Topas as mass vs intensity, and the
192 O_2^+ (31.99 Da) peak was fitted with a split Pearson VII peak shape and a constant background
193 between 31.6 and 32.6 Da in order to avoid the small peaks at mass 33 and 34 Da (Fig. 4). This
194 model was weighted based on counting statistics. Once the peak fitting model had converged,
195 the peak $M/\Delta M_{10}$ at 95% confidence (2 sigma) was calculated.

196 4. Results

197 4.1. Chemical and physical parameter variation with laser energy

198 All datasets investigated appeared homogeneous at the nanoscale and no clusters were
199 observed in the studied standards. Therefore, no emphasis was placed on the effect of clusters
200 as observed in granulite facies monazite grains of the Sandmata complex (India; (Fougerouse
201 et al., 2018)) and the rogaland complex (Norway; (Seydoux-Guillaume et al., 2019)).

202 The sequential analysis of specimen M1 and M2 (M1-1 to M1-7 and M2-1 to M2-7) reveals the
203 effect of laser energy on various measurement parameters (Fig. 5). The proportion of two
204 charge states of an ion can be used as a proxy measurement of the electric field during analysis.
205 For individual specimen, the $\text{La}^{+++}/\text{La}^{++}$ ratio is similar at same laser energies but different
206 voltages (M1: 6.1 kV and 6.8 kV at 300 pJ; M2: 6.5 kV and 7.5 kV at 300 pJ) suggesting a small
207 influence of the voltage on the electric field. However, the $\text{La}^{+++}/\text{La}^{++}$ ratio is negatively
208 correlated with the laser energy for both M1 and M2 and indicates that the field is weaker at
209 stronger laser energies. The $^{208}\text{Pb}^{++}$ counts decrease at higher laser power in specimen M1,
210 however such decrease is not observed for specimen M2. The decrease in $^{208}\text{Pb}^{++}$ counts in M1
211 is correlated with the increase of $^{208}\text{Pb}^{+}$ counts, which is consistent with a weaker field at high
212 laser energies. In opposition, the ThO^{++} counts are correlated with increasing laser energy for
213 M1 and M2. The $M/\Delta M_{10}$ value also increases with higher laser energies indicating that the
214 peak is narrower at higher laser energy. These experiments indicate a positive correlation, and
215 a possibly useful relationship, between the measured ThO^{++} counts and $M/\Delta M_{10}$.

216 During these experiments, the same specimen at the same laser energy, but different voltages,
217 did not provide comparable results. For example at a constant 300 pJ laser energy but higher
218 average voltage, the ThO^{++} counts change by +2.2% between M1-5 and M1-7, and -2.2%
219 between M2-4 and M2-7.

220 4.2. Molecular fractionation and peak shape

221 To test the relationship between fractionation and peak shape, we have used all of the data
222 and have selected a subset of the large datasets in order to have comparable dataset sizes. To
223 crop the large datasets, we selected a 40 nm slice (~ 5 million ions) at approximately
224 equidistance from the top and bottom of the reconstructed volume. Using all standards,
225 irrespective of age or Th content, a correlation is apparent between the $^{208}\text{Pb}/^{232}\text{Th}$ fractionation
226 and $M/\Delta M_{10}$ parameter (Fig. 6). A linear regression through these variables yields $y =$
227 $0.381(\pm 0.048)x - 255(\pm 26)$ with a coefficient of determination (R^2) of 0.761. A prediction interval
228 is an estimate of an interval in which a future observation will fall, with a 95% probability
229 (Geisser, 1993). For any value within the range of $M/\Delta M_{10}$ measured, it is possible to calculate
230 the 95% prediction interval for the mean value of y (\hat{y}) using equation (3):

231
$$\hat{y} \pm t_{\alpha/2} \cdot SE \cdot \sqrt{1 + \frac{1}{n} + \frac{(x - \bar{x})^2}{(n-1) \cdot S_x^2}} \quad (\text{eq. 3})$$

232 With $t_{\alpha/2}$ the t-statistic parameter for 95% confidence, SE the standard error, n the number of
 233 observations, \bar{x} and S_x^2 the mean and sample variance of all standards $M/\Delta M_{10}$ values,
 234 respectively.

235

236 4.3. Peak shape variation with voltage

237 To investigate the effect that voltage has on the measured peak shape and fractionation, one
 238 large dataset was studied in detail (100 million atoms; specimen M4 - Moacyr). The dataset
 239 was cropped using the voltage evolution curve in five even sections of 20 million ions and
 240 each section was reconstructed independently (Fig. 7A&B). Finally, an additional five subset
 241 were cropped using a 50 nm wide region of interest from the reconstructed atom map at
 242 various voltages across the dataset (Fig. 7A). The voltage range was estimated by subtracting
 243 the lowest voltage value from the highest value for each subset (delta voltage). The voltage
 244 range decreased progressively within the subset succession. The smallest range were
 245 measured for the 50 nm subsets (Fig 7C). The $M/\Delta M_{10}$ values for each subset are anti-
 246 correlated with the voltage range (Fig. 7C) with the $M/\Delta M_{10}$ parameter decreasing with an
 247 increasing voltage range. This correlation is expected because the post-acquisition calibration
 248 of the data correct first-order variability in time-of-flight (and thus mass-to-charge state ratios)
 249 due to changes in voltage (Sebastian et al., 2001). The variation of the $M/\Delta M_{10}$ parameter with
 250 voltage range is also apparent when plotted against fractionation with higher voltage range
 251 values resulting in higher dispersion from the $^{208}\text{Pb}/^{232}\text{Th}$ fractionation and $M/\Delta M_{10}$ correlation
 252 line (Fig. 7D).

253 The average voltage dependence on the $M/\Delta M_{10}$ parameter and fractionation is however less
 254 clear. In exception of the lowest voltage subset that has a large voltage range (white box on
 255 Fig 7A), the other 50 nm subregions cluster at similar $M/\Delta M_{10}$ values and no systematic
 256 relationship between $M/\Delta M_{10}$ values and voltage is apparent. The measured fractionation
 257 values are also similar at different voltages (Fig. 7D).

258 5. Discussion

259 5.1. Effect of instrument parameters on data quality

260 The ratio of two different charge states of one ionic species is commonly used as a proxy for
261 the strength of the electric field during atom probe analysis (Kingham, 1982). In monazite, the
262 $\text{La}^{+++}/\text{La}^{++}$ ratio decreases with increasing laser energy (Fig. 5). This relationship is interpreted
263 to be the result of lower field strength occurring at higher laser energy. In geological materials,
264 similar observations have been made for zircon (La Fontaine et al., 2017; Saxey et al., 2018),
265 however the opposite relationships have been observed for rutile (Verberne et al., 2019) and
266 magnetite (Schreiber et al., 2014).

267 The weaker field with increasing laser energy also affects the $^{208}\text{Pb}^{++}$ and ThO^{++} counts. With
268 lower field, the $^{208}\text{Pb}^{++}$ counts significantly decrease for specimen M1 (C-83-32). However,
269 $^{208}\text{Pb}^{++}$ counts remained relatively constant for specimen M2 (B0109G; Fig. 5). Two possible
270 scenarios can explain this observation. The first scenario is that the field varied in smaller
271 amounts in specimen 2 than in specimen 1. This seems unlikely because the $\text{La}^{+++}/\text{La}^{++}$ ratio
272 varies in a similar fashion for both specimens. Alternatively, the compositional difference
273 between the two standards may influence the ionic evaporation of Pb. However, this theory
274 needs further testing with additional analyses.

275 In contrast, the ThO^{++} counts increases by up to 40% for M1 (M1-1 to M1-7) and 20% for M2
276 (M2-1 to M2-7; Fig. 5), indicating that higher laser energy and lower field has a strong effect
277 on ThO^{++} counts. Molecular ion formation is generally prevalent in lower fields (Kirchhofer et
278 al., 2013), suggesting that ThO can be more affected by the field conditions than Pb in
279 monazite. Several Th-bearing ionic species have been identified in the mass spectra of
280 monazite (ThO^{++} , ThPO_3^{+++} , ThPO_4^{++} , $\text{ThP}_2\text{O}_6^{+++}$; (Fougereuse et al., 2018)). However, when
281 encompassing all identified peaks at a given laser energy, the Th content remains largely
282 underestimated (Fougereuse et al., 2018; Seydoux-Guillaume et al., 2019). A missing Th ionic
283 molecule could cause this underestimation. Given the complexity of the monazite mass
284 spectra (Fig. 3), it is likely that an unidentified Th-bearing species could be overlapping with
285 another major molecular species. The observation that ThO^{++} increases with a decreasing field
286 suggests that the missing molecule could be triply-charged. Doubly-charged molecules would
287 preferentially form at the detriment of triply-charged molecules in lower field conditions
288 (Kingham, 1982). A potential candidate is ThPO_4^{+++} overlapping with LaPO_3^{++} at ~109 Da.

289 The various plots in figure 5 show the effect of some analysis parameters on the measured
290 chemical makers. The voltage range experiment (Fig. 7) indicates that the specimen voltage
291 and therefore specimen shape, only play a minor role in the measured $^{208}\text{Pb}^{++}$ and ThO^{++}
292 counts. At fixed laser energy, but different voltage, the ThO^{++} counts varied by +2.2% and -
293 2.2% in the two specimens investigated (Fig. 5).

294 Another factor responsible for the ThO^{++} increase is higher mass resolution. The methodology
295 to quantify the ThO^{++} counts rely on measuring the counts within a narrow range (0.1 Da),
296 below the centre of the peak, at its maximum height. A higher mass resolving power ($M/\Delta M_{10}$)
297 indicates that the peak is narrower and therefore higher at equal signal. The observation that
298 $M/\Delta M_{10}$ increases with higher laser energy suggests that the ThO^{++} counts will increase in
299 proportion to the laser energy. However, the increase in the $M/\Delta M_{10}$ is unlikely sufficient to
300 account for the 40% increase in ThO^{++} counts on its own. Hence, it is likely that the observation
301 of increasing ThO^{++} counts at higher laser energy is due to the combined effect of preferential
302 ThO^{++} formation to detriment of other triply-charged molecules and higher mass resolving
303 power ($M/\Delta M_{10}$) values.

304 In our data, the $M/\Delta M_{10}$ peak parameter increases with laser energy. This trend is opposite to
305 the trend observed in Zircon and Rutile (Saxey et al., 2018; Verberne et al., 2019) but is similar
306 to what is observed in tungsten carbide (Peng et al., 2017) although it is unclear what effects
307 the laser stepping protocol may have on peak shape. In monazite, we demonstrated that at
308 higher laser power, the field at the apex of the specimen is reduced, suggesting that less
309 spontaneous evaporation would occur between pulses and this could be the explanation for
310 the narrower peaks.

311 5.2. Monazite $^{208}\text{Pb}/^{232}\text{Th}$ geochronology by atom probe tomography

312 The radioactive decay of a radionuclide is characterised by its half-life constant. Such a
313 characteristic is based on a probability function and the half-life of a radioactive element is
314 therefore most accurate for an infinite number of atoms. In the case of $^{208}\text{Pb}/^{232}\text{Th}$
315 nanogeochronology described here, we have used volumes that encompass between 15,000
316 and 100,000 ^{232}Th atoms, in which volume half-life is still a viable concept.

317 Using the linear correlation between the $^{208}\text{Pb}/^{232}\text{Th}$ fractionation coefficient and the $M/\Delta M_{10}$
318 peak parameter, it is possible to use atom probe tomography to measure unknown monazites
319 and derive a $^{208}\text{Pb}/^{232}\text{Th}$ age. The $M/\Delta M_{10}$ value (x) measured for any atom probe data can be
320 used to predict a $^{208}\text{Pb}/^{232}\text{Th}$ fractionation factor (y) using $y = 0.381(\pm 0.048)x - 255(\pm 26)$. The
321 error propagation of the prediction is given by the uncertainty of the $M/\Delta M_{10}$ value, the
322 uncertainty of the measured $^{208}\text{Pb}/^{232}\text{ThO}$ ratio and the 95% prediction band of the calibration
323 defined by equation (3).

324 In atom probe data, the uncertainty on $^{208}\text{Pb}/^{232}\text{Th}$ age is limited by counting statistics, and
325 background and fractionation corrections. The counting statistics and background correction
326 indicates that the maximum precision attainable for a dataset larger than 5 million atoms is
327 1.5 to 2% (2σ) on individual analyses. To test the effect of the fractionation correction on the
328 $^{208}\text{Pb}/^{232}\text{Th}$ age precision and accuracy, the methodology has been applied on the same datasets
329 used for this study. For dataset M9 (Manangotry 555 ± 2 Ma; (Paquette and Tiepolo, 2007)), an
330 arbitrary 50 nm slice in the middle of the dataset was cropped from the reconstructed 3d atom
331 map (Fig. 7). The $M/\Delta M_{10}$ parameter is 554.2 ± 1.8 , yielding a predicted $^{208}\text{Pb}/^{232}\text{Th}$ fractionation
332 coefficient of -43.3 ± 6.7 %. Using the measured $^{208}\text{Pb}/^{232}\text{ThO}$ ratio of 0.0486 ± 0.0017 , a
333 fractionation corrected $^{208}\text{Pb}/^{232}\text{Th}$ ratio of 0.0276 ± 0.004 is calculated for an age of 550 ± 86 Ma
334 (2 sigma). The predicted age is in good agreement with the published age of 555 ± 2 Ma
335 (Paquette et al., 1994), with uncertainties on the order of 16% at 2 sigma for a for a subset of
336 an atom probe data set having a volume of approximately $0.0007 \mu\text{m}^3$. By comparison,
337 monazite SIMS analyses have typically uncertainties in the order of 1 to 2% for a volume of
338 $<10 \mu\text{m}^3$. Calculating weighted mean average fractionation corrected $^{208}\text{Pb}/^{232}\text{Th}$ ages for each
339 standard (Fig. 8; one data point per atom probe analysis), yields 551 ± 51 Ma ($n = 3$; MSWD =
340 0.046; probability = 0.95) for Manangotry (555 ± 2 Ma (Paquette et al., 1994)), 1136 ± 74 Ma (n
341 = 8; MSWD = 0.32; probability = 0.94) for B0109G (1137 ± 1 Ma; (Bingen et al., 2008)) and 2707
342 ± 150 Ma ($n = 7$; MSWD = 0.55; probability = 0.77) for C-83-32 ($2,685 \pm 2$ Ma; (Corfu, 1988)). No
343 weighted mean average is calculated for DIG19 and Moacyr as only two and one dataset for
344 each standard was acquired, respectively.

345 5.3. Recommendations

346 To obtain reliable isotopic information from atom probe measurements of monazite, several
347 parameters can be optimised, in particular for $^{208}\text{Pb}/^{232}\text{Th}$ chronology. ThO^{++} counts increase
348 with laser energy, in contrast $^{208}\text{Pb}^{++}$ counts decrease with laser energy. However, the
349 uncertainty on the counting statistics of the $^{208}\text{Pb}/\text{ThO}^{++}$ ratio improve at higher laser energy.
350 In contrast, the uncertainties characterizing the $M/\Delta M_{10}$ peak parameter, which is used to
351 correct the molecular fractionation, is not systematically affected by laser energy. These
352 relationships indicate that laser energy in the 200 to 400 pJ range is optimal. Monazites with
353 low ^{208}Pb content (young or low-Th crystals) may require further optimization of running
354 conditions in order to maximise the $^{208}\text{Pb}^{++}$ peak. In the latter case, low laser power in the 50
355 to 100 pJ range may be more appropriate.

356 Holding laser energy constant, the voltage applied to the atom probe needle affects the
357 $M/\Delta M_{10}$ fractionation parameter. A smaller range of voltage results in a more reliable peak
358 shape quantification and we recommend use of a subsection of any atom probe dataset where
359 the voltage range is limited to ensure reproducibility. We have found that a 40 to 50 nm
360 portion of the entire dataset, or a 5 million ion subset, to work well in $^{208}\text{Pb}/^{232}\text{Th}$
361 geochronology of monazite. Also, to minimize the voltage change during data acquisition,
362 specimens may be prepared with low shank angles, and data collected only after the initial
363 shaping of the tip has completed and the voltage is increasing more slowly (Fig 7).

364 Datasets presenting Pb-rich cluster can also be investigated (Fougerouse et al., 2018; Seydoux-
365 Guillaume et al., 2019). From the same subset, as defined above, the age of clusters and matrix
366 can be measured together, or the matrix can be sub-sampled and measured separately. This
367 approach can potentially provide additional information about the history of the crystal and
368 mechanisms for Pb mobility (Fougerouse et al., 2019).

369 The derivation of a physically realistic model of the peak shape and associated background
370 would allow for the modelling of entire sections of a spectrum and potentially would allow
371 for a more precise extractions of isotopic abundances.

372 As shown in our data, the fractionation correction protocol defined in this study can be
373 applied over a range of monazite composition, specimen shape (no dependence on voltage)
374 and laser energy. Such benefits are desirable for APT in order to adjust the acquisition
375 parameters based on the data quality for individual samples.

376 6. Case study: dating the contact metamorphism of the Fanad granite, Ireland

377 The granites of the Donegal region in the North of Ireland represent a classic example of a
378 range of granite emplacement mechanisms (Pitcher and Berger, 1972). These intrusions
379 formed during the Early Devonian, at the close of the Caledonian Orogeny between c. 418 to
380 397 Ma, and were in the main emplaced into a major SW-NE trending sinistral shear zone
381 system (Kirkland et al., 2008). The Fanad pluton is an important constituent of the Donegal
382 granites that has yielded a Rb-Sr isochron age of 402 ± 10 Ma, interpreted as the magmatic
383 crystallization age (O'Connor et al., 1987). Petrographically the granite is mainly coarse
384 grained and sometimes porphyritic granodiorite, but it ranges to monzogranite, monzonite
385 and monzodiorite. Pitcher and Berger (1972) indicate that the Fanad pluton was emplaced into
386 metasediments of the Ards Quartzite Formation, Neoproterozoic Dalradian Supergroup
387 (Berger, 1980). The country rock consists of well-bedded and massive feldspathic quartzites
388 and pelites (Fig 9A). In pelites close to the batholith, numerous small monazite grains are
389 present, often developed as inclusions within prograde metamorphic biotite crystals. We
390 interpret these textural relationships as consistent with crystallisation of monazite during
391 contact metamorphism associated with emplacement of the Fanad granite.

392 To determine an age on these minute monazite crystals a $6 \times 2 \mu\text{m}$ grain was analysed by atom
393 probe. The investigated monazite sits as an inclusion within a biotite grain (Fig. 9B), some 990
394 metres from the intrusion contact with pelites as measured from the present day land surface.
395 This monazite was selected because it was possible to prepare three atom probe specimens
396 from it, although smaller grains could have also been analysed (Fig. 9C). The three atom probe
397 specimens yielded 15, 15 and 40 million ions, with measured $^{208}\text{Pb}/^{232}\text{Th}$ ratios of 0.038 ± 0.004 ,
398 0.036 ± 0.004 and 0.035 ± 0.005 and $M/\Delta M_{10}$ values of 550.7 ± 2.3 , 555.5 ± 2.3 and 565.9 ± 2.1 ,
399 respectively. Using the protocol established in this study, corrected $^{208}\text{Pb}/^{232}\text{Th}$ ages are $419 \pm$
400 101 Ma, 412 ± 98 Ma and 434 ± 124 Ma, which define a weighted mean age of 420 ± 60 Ma (Fig.
401 9; $n = 3$; MSWD = 0.040; probability = 0.96). The weighted mean monazite age is consistent
402 with the anticipated age of contact metamorphism associated with the intrusion of the Fanad
403 pluton.

404 7. Conclusion

405 In this study we define a protocol to correct fractionation in atom probe analysis between
406 $^{232}\text{ThO}^{++}$ and $^{208}\text{Pb}^{++}$ in monazite crystals with sample volumes $<0.0007 \mu\text{m}^3$. The methodology
407 we have developed is by far the highest spatial resolution technique for isotope
408 geochronology of monazite. The $M/\Delta M_{10}$ peak shape parameter appears to adequately
409 characterise the degree of molecular fractionation to allow results that can address a range of
410 geologically pertinent questions. The uncertainties calculated on ages using this method take
411 into account counting statistics, background correction, and fractionation effects. The
412 uncertainty on the fractionation corrected $^{208}\text{Pb}/^{232}\text{Th}$ ratio is currently between 15 and 20 % (2
413 σ). Instrument running parameters can be optimised for nanogeochronology of monazite with
414 the laser energy in the range 200 to 400 pJ and limiting large datasets to c. 50 nm wide crops
415 to curtail the range of voltages applied to the specimen during analysis. This new technique
416 opens up the potential to date small monazite grains and grain domains which have hitherto
417 been vastly below the spatial resolution of geochronology.

418

419 **Availability of data**

420 The data that support the findings of this study are available on request from the
421 corresponding author. The data are not publicly available due to privacy or ethical
422 restrictions.

423 **Acknowledgments**

424 The Australian Resource Characterisation Facility (ARCF), under the auspices of the National
425 Resource Sciences Precinct (NRSP) – a collaboration between CSIRO, Curtin University and
426 The University of Western Australia – is supported by the Science and Industry Endowment
427 Fund (SIEF RI13-01). The authors gratefully acknowledge support of Curtin University's
428 Microscopy & Microanalysis Facility and the John de Laeter Centre, whose instrumentation
429 has been supported by University, State and Commonwealth Government funding. DF
430 acknowledges ARC funding DE190101307.

431

432 **Figure captions:**

433 Table 1: Table 1: Reference material composition and age in wt.%; 1: Seydoux-Guillaume et
434 al., 2002; 2: Seydoux-Guillaume et al., 2004; 3: Paquette et al., 1994; 4: Schärer and Deutsch,
435 1990; 5: Corfu, 1988; 6: Didier, 2013; 7: Bingen et al., 2008; 8: Kirkland et al., 2009.

436 Table 2: Standard description, APT analytical parameters and results.

437 Figure 1: Comparative analysis volumes for selected dating techniques. ID-TIMS: Isotopic
438 Dilution - Thermal Ionization Mass Spectrometry; LA-ICPMS: Laser Ablation - Inductively
439 Coupled Plasma Mass Spectrometry; SIMS: Secondary Ion Mass Spectrometry; EPMA:
440 Electron Probe Microanalyser. Left side panel: each volumes are represented on a schematic
441 monazite grain (diagram to scale).

442 Figure 2: A) SEM image of a monazite atom probe specimen; B) 3-D APT atom map. Only
443 $^{232}\text{ThO}^{++}$ and $^{208}\text{Pb}^{++}$ atoms are displayed; C) Voltage evolution curve during APT analysis. The
444 voltage increases to compensate for the specimen radius increase.

445 Figure 3: A) APT Mass-to-charge spectra of monazite. Close up for $^{208}\text{Pb}^{++}$ (B) and $^{232}\text{ThO}^{++}$ (C).

446 Figure 4: Example of the peak fitting result of the O_2^+ peak for one dataset. The black line is
447 the experimental data and the red line is the fit. The $M/\Delta M_{10}$ is given by the position of the O_2^+
448 peak divided by the full-width-at-tenth-maximum (FWTM).

449 Figure 5: Sequential analysis of specimen M1 (C-83-32; blue) and M2 (B0109G; yellow). The
450 voltage value is the average voltage between the start and the end of the analysis. Error bars
451 are smaller than the symbols. A) $^{208}\text{Pb}^{++}$ counts normalised to 1 million atoms; B) $\text{La}^{+++}/\text{La}^{++}$
452 ratio for each analysis; C) $^{232}\text{ThO}^{++}$ counts normalised to 1 million atoms; D) $M/\Delta M_{10}$ peak
453 shape parameter for each analysis.

454 Figure 6: $M/\Delta M_{10}$ peak shape parameter in function of $^{232}\text{ThO}/^{208}\text{Pb}$ fractionation (%) for all
455 standards. The data are correlated and is defined by $y = 0.381(\pm 0.048)x - 255(\pm 26)$ with a
456 coefficient of determination (R^2) of 0.761. The dark grey area represents the 95% confidence
457 band and the light grey area the 95% prediction band.

458 Figure 7: Effect of voltage on data quality for specimen M4 (Moacyr). A and B) Sequential
459 reconstruction by 20 million ions subsets (colour coded) and 50 nm subregions (grayscale
460 coded). The subsets on A and B are colour coded for C and D; C) Voltage range (delta voltage)

461 plotted against the $M/\Delta M_{10}$ peak parameter. The peaks broaden when the range of voltage
462 applied to the specimen during analysis increases; D) $M/\Delta M_{10}$ peak parameter plotted against
463 the fractionation (%). The higher voltage range values result in higher dispersion from the
464 $^{208}\text{Pb}/^{232}\text{Th}$ fractionation and $M/\Delta M_{10}$ correlation line.

465 Figure 8: Raw data (squares) and corrected (circles) $^{208}\text{Pb}/^{232}\text{Th}$ ages for (A) Manangotry, (B)
466 B0109G and (C) C-83-32. The uncertainties are given at 2 sigma. The weighted mean average
467 ages are in good agreement with the published standard ages.

468 Figure 9: A) Simplified geological map of the Fanad granite and host metasediments (Donegal
469 region, Ireland). The sample location from the pelites is indicated with a star; B) Micrograph
470 of the monazite grain selected for this study. Three atom probe specimen were prepared from
471 the $6 \times 2 \mu\text{m}$ grain; C) Monazite grain size (diameter) distribution in the thin section studied.
472 The bin size is $1 \mu\text{m}$; D) Raw data (squares) and corrected (circles) $^{208}\text{Pb}/^{232}\text{Th}$ ages. The $420 \pm$
473 60 Ma weighted mean average age is consistent with the Fanad pluton contact metamorphism.

474 **References**

- 475 Allaz, J., Selleck, B., Williams, M.L., and Jercinovic, M.J. (2013) Microprobe analysis and dating
476 of monazite from the Potsdam Formation, New York: A progressive record of chemical
477 reaction and fluid interaction. *American Mineralogist*, 98(7), 1106-1119.
- 478 Audi, G., Bersillon, O., Blachot, J., and Wapstra, A. (2003) The NUBASE evaluation of nuclear
479 and decay properties. *Nuclear Physics A*, 729(1), 3-128.
- 480 Berger, A. (1980) The structural setting of the Main Donegal Granite; comments on a recent
481 interpretation. *Geological Journal*, 15(1), 3-6.
- 482 Bingen, B., Davis, W.J., Hamilton, M.A., Engvik, A.K., Stein, H.J., Skår, Ø., and Nordgulen, Ø.
483 (2008) Geochronology of high-grade metamorphism in the Sveconorwegian belt, S.
484 Norway: U-Pb, Th-Pb and Re-Os data. *Norwegian Journal of Geology/Norsk*
485 *Geologisk Forening*, 88(1).
- 486 Coelho, A.A. (2018) TOPAS and TOPAS-Academic: an optimization program integrating
487 computer algebra and crystallographic objects written in C++. *Journal of Applied*
488 *Crystallography*, 51(1), 210-218.
- 489 Corfu, F. (1988) Differential response of U-Pb systems in coexisting accessory minerals,
490 Winnipeg River Subprovince, Canadian Shield: implications for Archean crustal
491 growth and stabilization. *Contributions to Mineralogy and Petrology*, 98(3), 312-325.
- 492 Erickson, T., Pearce, M., Taylor, R., Timms, N.E., Clark, C., Reddy, S., and Buick, I. (2015)
493 Deformed monazite yields high-temperature tectonic ages. *Geology*, 43(5), 383-386.
- 494 Fletcher, I.R., McNaughton, N.J., Davis, W.J., and Rasmussen, B. (2010) Matrix effects and
495 calibration limitations in ion probe U-Pb and Th-Pb dating of monazite. *Chemical*
496 *Geology*, 270(1-4), 31-44.
- 497 Fougereuse, D., Reddy, S.M., Kirkland, C.L., Saxey, D.W., Rickard, W.D., and Hough, R.M.
498 (2019) Time-resolved, defect-hosted, trace element mobility in deformed
499 Witwatersrand pyrite. *Geoscience Frontiers*, 10(1), 55-63.
- 500 Fougereuse, D., Reddy, S.M., Saxey, D.W., Erickson, T.M., Kirkland, C.L., Rickard, W.D.A.,
501 Seydoux-Guillaume, A.M., Clark, C., and Buick, I.S. (2018) Nanoscale distribution of
502 Pb in monazite revealed by atom probe microscopy. *Chemical Geology*, 479, 251-258.
- 503 Gasquet, D., Bertrand, J.-M., Paquette, J.-L., Lehmann, J., Ratzov, G., De Ascensão Guedes, R.,
504 Tiepolo, M., Boullier, A.-M., Scaillet, S., and Nomade, S. (2010) Miocene to Messinian

505 deformation and hydrothermal activity in a pre-Alpine basement massif of the French
506 western Alps: new U-Th-Pb and argon ages from the Lauzière massif. *Bulletin de la*
507 *Société Géologique de France*, 181(3), 227-241.

508 Geisser, S. (1993) *Predictive Inference*. New York: Routledge.

509 Grand'Homme, A., Janots, E., Seydoux-Guillaume, A.-M., Guillaume, D., Bosse, V., and
510 Magnin, V. (2016) Partial resetting of the U-Th-Pb systems in experimentally altered
511 monazite: Nanoscale evidence of incomplete replacement. *Geology*, 44(6), 431-434.

512 Grove, M., and Harrison, T. (1999) Monazite Th-Pb age depth profiling. *Geology*, 27(6), 487-
513 490.

514 Janots, E., Berger, A., Gnos, E., Whitehouse, M., Lewin, E., and Pettke, T. (2012) Constraints
515 on fluid evolution during metamorphism from U-Th-Pb systematics in Alpine
516 hydrothermal monazite. *Chemical Geology*, 326, 61-71.

517 Janots, E., Engi, M., Berger, A., Allaz, J., Schwarz, J.O., and Spandler, C. (2008) Prograde
518 metamorphic sequence of REE minerals in pelitic rocks of the Central Alps:
519 implications for allanite-monazite-xenotime phase relations from 250 to 610 C. *Journal*
520 *of Metamorphic Geology*, 26(5), 509-526.

521 Kingham, D.R. (1982) The post-ionization of field evaporated ions: A theoretical explanation
522 of multiple charge states. *Surface Science*, 116(2), 273-301.

523 Kirchhofer, R., Teague, M.C., and Gorman, B.P. (2013) Thermal effects on mass and spatial
524 resolution during laser pulse atom probe tomography of cerium oxide. *Journal of*
525 *Nuclear Materials*, 436(1), 23-28.

526 Kirkland, C., Alsop, G., and Prave, A. (2008) The brittle evolution of a major strike-slip fault
527 associated with granite emplacement: a case study of the Leannan Fault, NW Ireland.
528 *Journal of the Geological Society*, 165(1), 341-352.

529 Kirkland, C.L., Fougereuse, D., Reddy, S.M., Hollis, J., and Saxey, D.W. (2018) Assessing the
530 mechanisms of common Pb incorporation into titanite. *Chemical Geology*, 483, 558-
531 566.

532 Kirkland, C.L., Whitehouse, M.J., and Slagstad, T. (2009) Fluid-assisted zircon and monazite
533 growth within a shear zone: a case study from Finnmark, Arctic Norway.
534 *Contributions to Mineralogy and Petrology*, 158(5), 637-657.

535 La Fontaine, A., Piazzolo, S., Trimby, P., Yang, L., and Cairney, J.M. (2017) Laser-Assisted Atom
536 Probe Tomography of Deformed Minerals: A Zircon Case Study. *Microscopy and*
537 *Microanalysis*, 23(2), 404-413.

538 Larson, D.J., Prosa, T., Ulfig, R.M., Geiser, B.P., and Kelly, T.F. (2013) Local electrode atom
539 probe tomography. New York, US: Springer Science.

540 Laurent, A.T., Duchene, S., Bingen, B., Bosse, V., and Seydoux-Guillaume, A.M. (2018) Two
541 successive phases of ultrahigh temperature metamorphism in Rogaland, S. Norway:
542 Evidence from Y-in-monazite thermometry. *Journal of Metamorphic Geology*, 36(8),
543 1009-1037.

544 Montel, J.-M., Razafimahatratra, D., De Parseval, P., Poitrasson, F., Moine, B., Seydoux-
545 Guillaume, A.-M., Pik, R., Arnaud, N., and Gibert, F. (2018) The giant monazite crystals
546 from Manangotry (Madagascar). *Chemical Geology*, 484, 36-50.

547 O'Connor, P., Long, C., and Evans, J. (1987) Rb-Sr whole-rock isochron studies of the
548 Barnesmore and Fanad plutons, Donegal, Ireland. *Geological Journal*, 22(1), 11-23.

549 Paquette, J.-L., Nédélec, A., Moine, B., and Rakotondrazafy, M. (1994) U-Pb, single zircon Pb-
550 evaporation, and Sm-Nd isotopic study of a granulite domain in SE Madagascar. *The*
551 *Journal of Geology*, 102(5), 523-538.

552 Paquette, J.-L., and Tiepolo, M. (2007) High resolution (5 μm) U-Th-Pb isotope dating of
553 monazite with excimer laser ablation (ELA)-ICPMS. *Chemical Geology*, 240(3), 222-
554 237.

555 Parrish, R.R. (1990) U-Pb dating of monazite and its application to geological problems.
556 *Canadian Journal of Earth Sciences*, 27(11), 1431-1450.

557 Peng, Z., Choi, P.-P., Gault, B., and Raabe, D. (2017) Evaluation of analysis conditions for laser-
558 pulsed atom probe tomography: example of cemented tungsten carbide. *Microscopy*
559 *and Microanalysis*, 23(2), 431-442.

560 Peterman, E.M., Reddy, S.M., Saxey, D.W., Snoeyenbos, D.R., Rickard, W.D., Fougereuse, D.,
561 and Kylander-Clark, A.R. (2016) Nanogeochronology of discordant zircon measured
562 by atom probe microscopy of Pb-enriched dislocation loops. *Science Advances*, 2(9),
563 e1601318.

564 Pitcher, W.S., and Berger, A.R. (1972) *The geology of Donegal: a study of granite emplacement*
565 *and unroofing*. John Wiley & Sons.

566 Poitrasson, F., Chenery, S., and Shepherd, T.J. (2000) Electron microprobe and LA-ICP-MS
567 study of monazite hydrothermal alteration:: Implications for U-Th-Pb geochronology
568 and nuclear ceramics. *Geochimica et Cosmochimica Acta*, 64(19), 3283-3297.

569 Reddy, S.M., Saxey, D.W., Rickard, W.D.A., Fougereuse, D., Montalvo, S.D., Verberne, R., and
570 van Riessen, A. (2020) Atom Probe Tomography: Development and Application to the
571 Geosciences. *Geostandards and Geoanalytical Research*, n/a(n/a).

572 Rickard, W.D.A., Reddy, S.M., Saxey, D.W., Fougereuse, D., Daly, L., Peterman, E., Timms,
573 N., Cavosie, A.J., and Jourdan, F. (2020) Novel Applications of FIB-based Techniques
574 in Atom Probe Tomography Workflows. *Microscopy and Microanalysis*.

575 Saxey, D., Reddy, S.M., Fougereuse, D., and Rickard, W.D. (2018) The Optimization of Zircon
576 Analyses by Laser-Assisted Atom Probe Microscopy: Insights from the 91500 Zircon
577 Standard. *Microstructural Geochronology: Planetary Records Down to Atom Scale*,
578 293-313.

579 Schärer, U., and Deutsch, A. (1990) Isotope systematics and shock-wave metamorphism: II. U-
580 Pb and Rb-Sr in naturally shocked rocks; the Haughton Impact Structure, Canada.
581 *Geochimica et Cosmochimica Acta*, 54(12), 3435-3447.

582 Schreiber, D.K., Chiamonti, A.N., Gordon, L.M., and Kruska, K. (2014) Applicability of post-
583 ionization theory to laser-assisted field evaporation of magnetite. *Applied Physics*
584 *Letters*, 105(24), 244106.

585 Sebastian, J.T., Hellman, O.C., and Seidman, D.N. (2001) New method for the calibration of
586 three-dimensional atom-probe mass spectra. *Review of Scientific Instruments*, 72(7),
587 2984-2988.

588 Seydoux-Guillaume, A.-M., Fougereuse, D., Laurent, A., Gardés, E., Reddy, S., and Saxey, D.
589 (2019) Nanoscale resetting of the Th/Pb system in an isotopically-closed monazite
590 grain: A combined atom probe and transmission electron microscopy study.
591 *Geoscience Frontiers*, 10(1), 65-76.

592 Seydoux-Guillaume, A.-M., Goncalves, P., Wirth, R., and Deutsch, A. (2003) Transmission
593 electron microscope study of polyphase and discordant monazites: Site-specific
594 specimen preparation using the focused ion beam technique. *Geology*, 31(11), 973-976.

595 Seydoux-Guillaume, A.-M., Montel, J.-M., Bingen, B., Bosse, V., De Parseval, P., Paquette, J.-
596 L., Janots, E., and Wirth, R. (2012) Low-temperature alteration of monazite: Fluid

597 mediated coupled dissolution–precipitation, irradiation damage, and disturbance of
598 the U–Pb and Th–Pb chronometers. *Chemical Geology*, 330, 140-158.

599 Seydoux-Guillaume, A.-M., Paquette, J.-L., Wiedenbeck, M., Montel, J.-M., and Heinrich, W.
600 (2002) Experimental resetting of the U–Th–Pb systems in monazite. *Chemical geology*,
601 191(1), 165-181.

602 Valley, J.W., Cavosie, A.J., Ushikubo, T., Reinhard, D.A., Lawrence, D.F., Larson, D.J., Clifton,
603 P.H., Kelly, T.F., Wilde, S.A., and Moser, D.E. (2014) Hadean age for a post-magma-
604 ocean zircon confirmed by atom-probe tomography. *Nature Geoscience*, 7(3), 219-223.

605 Valley, J.W., Reinhard, D.A., Cavosie, A.J., Ushikubo, T., Lawrence, D.F., Larson, D.J., Kelly,
606 T.F., Snoeyenbos, D.R., and Strickland, A. (2015) Presidential Address. Nano-and
607 micro-geochronology in Hadean and Archean zircons by atom-probe tomography and
608 SIMS: New tools for old minerals. *American Mineralogist*, 100(7), 1355-1377.

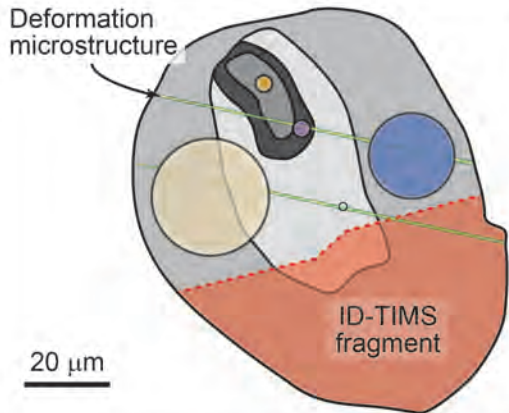
609 Verberne, R., Saxey, D.W., Reddy, S.M., Rickard, W.D., Fougereuse, D., and Clark, C. (2019)
610 Analysis of Natural Rutile (TiO₂) by Laser-assisted Atom Probe Tomography.
611 *Microscopy and Microanalysis*, 1-8.

612 Wawrzenitz, N., Krohe, A., Rhede, D., and Romer, R.L. (2012) Dating rock deformation with
613 monazite: The impact of dissolution precipitation creep. *Lithos*, 134, 52-74.

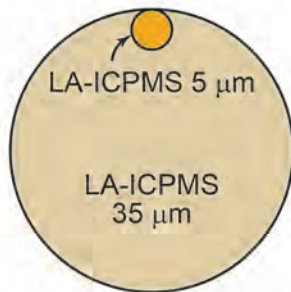
614 White, L.F., Darling, J., Moser, D., Reinhard, D., Prosa, T., Bullen, D., Olsen, D., Larson, D.,
615 Lawrence, D., and Martin, I. (2017) Atomic-scale age resolution of planetary events.
616 *Nature Communications*, 8, 1-6.

617 Yang, W., Lin, Y.-T., Zhang, J.-C., Hao, J.-L., Shen, W.-J., and Hu, S. (2012) Precise micrometre-
618 sized Pb-Pb and U-Pb dating with NanoSIMS. *Journal of Analytical Atomic*
619 *Spectrometry*, 27(3), 479-487.

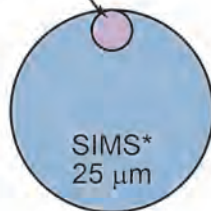
620



Top view



SIMS-NanoSIMS
5-3 μm



EPMA
2 μm

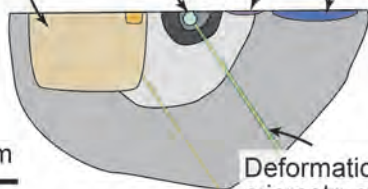


Atom probe specimen

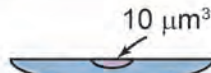
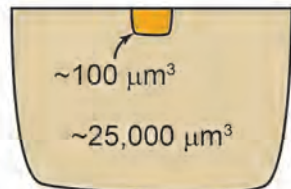
LA-ICPMS

EPMA

SIMS



Cross-section view

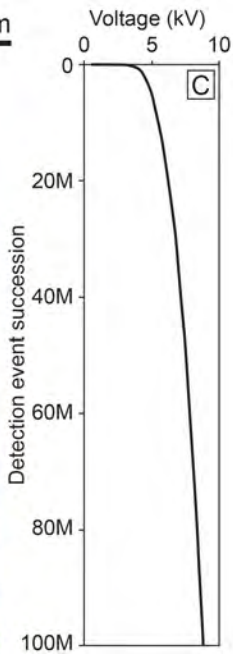
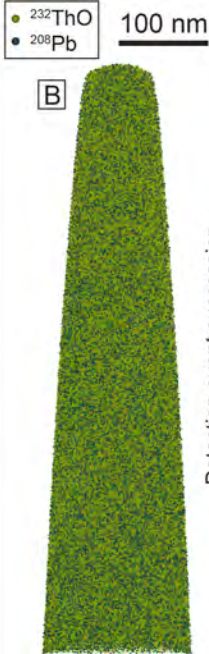


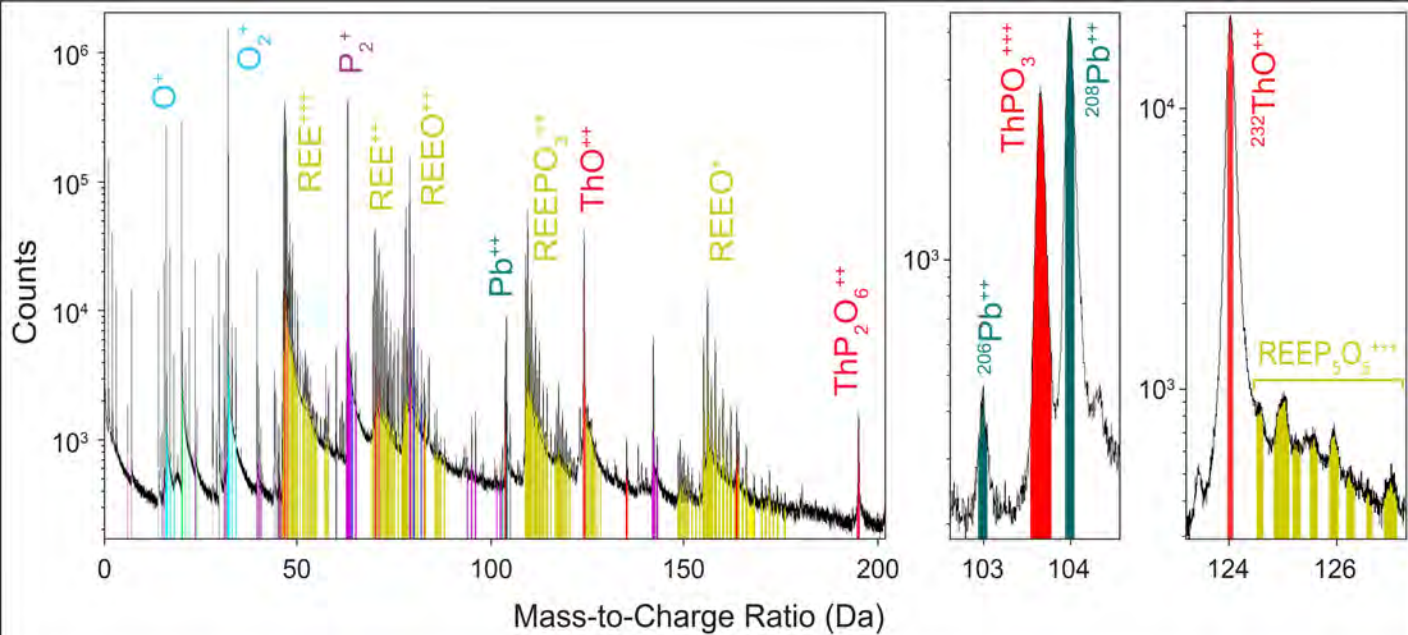
*2.5 μm^3 for SIMS
depth profiling

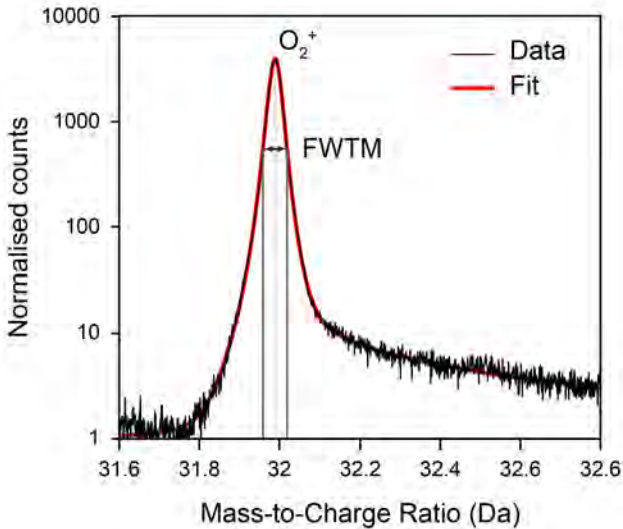


<35 μm^3

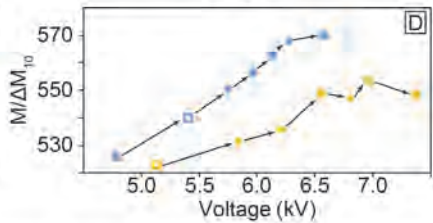
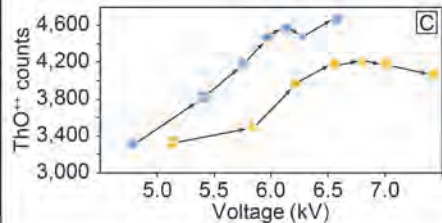
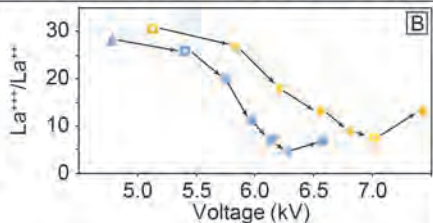
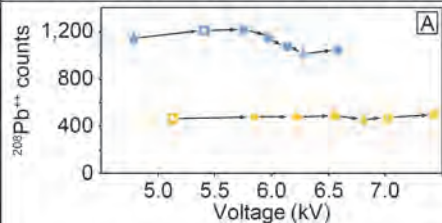
<0.008 μm^3

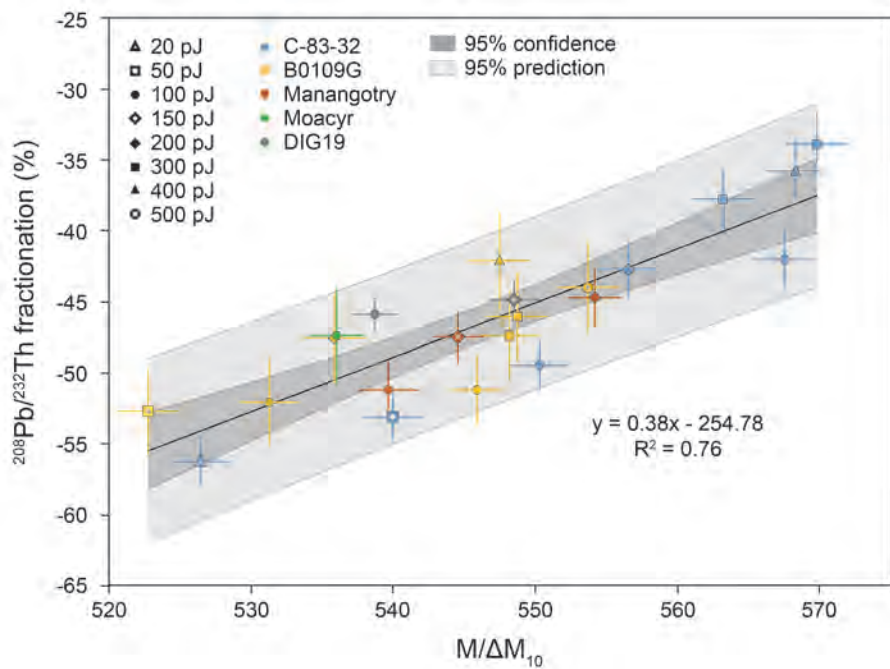


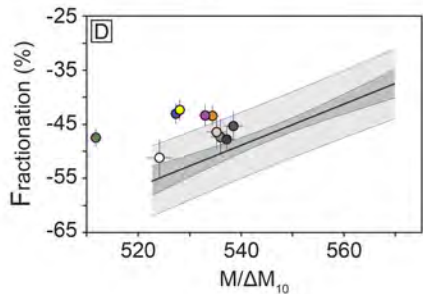
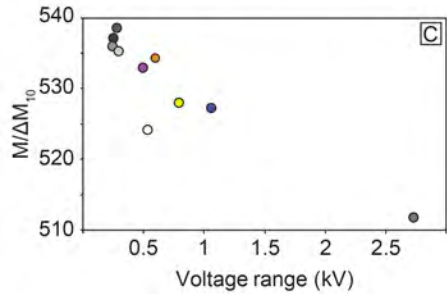
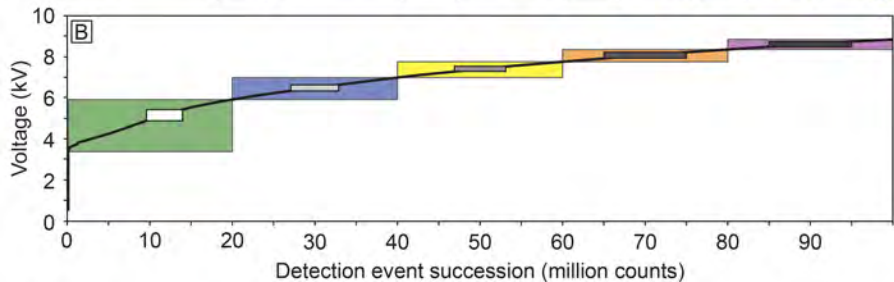




\blacktriangle 20 pJ \blacksquare 50 pJ \bullet 100 pJ \blacklozenge 200 pJ \blacksquare 300 pJ \blacktriangle 400 pJ \circ 500 pJ $\color{blue}\bullet$ C-83-32 $\color{orange}\bullet$ B0109G



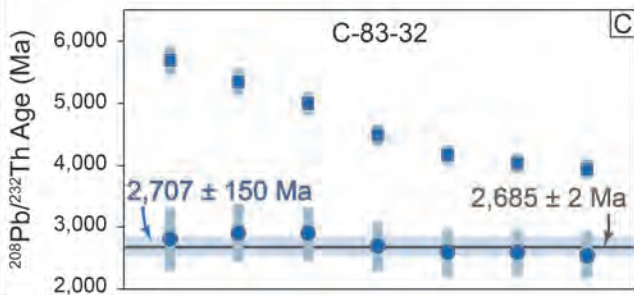
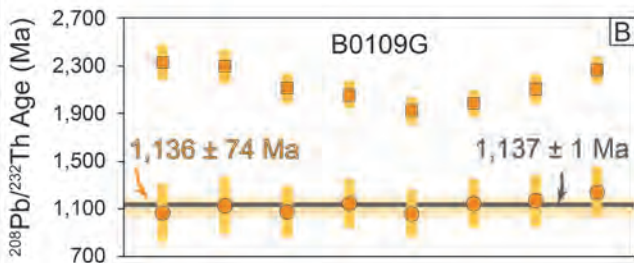
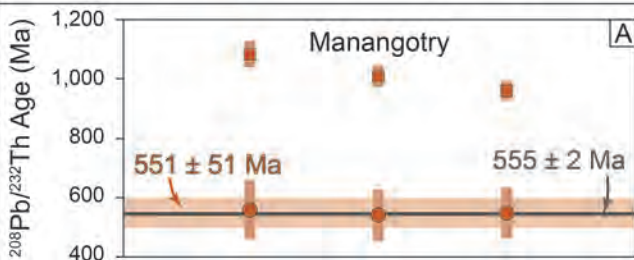


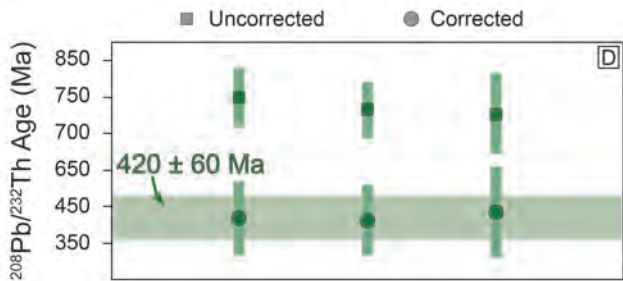
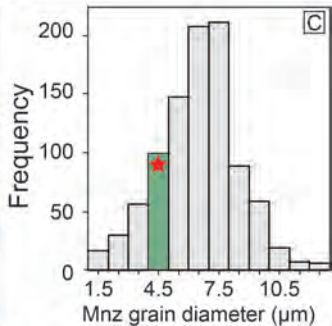
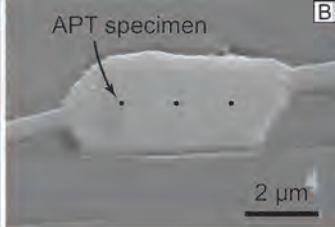
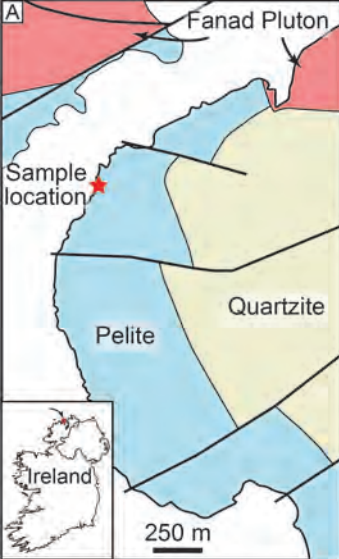


■ Uncorrected

● Corrected

| 2 sigma uncertainty





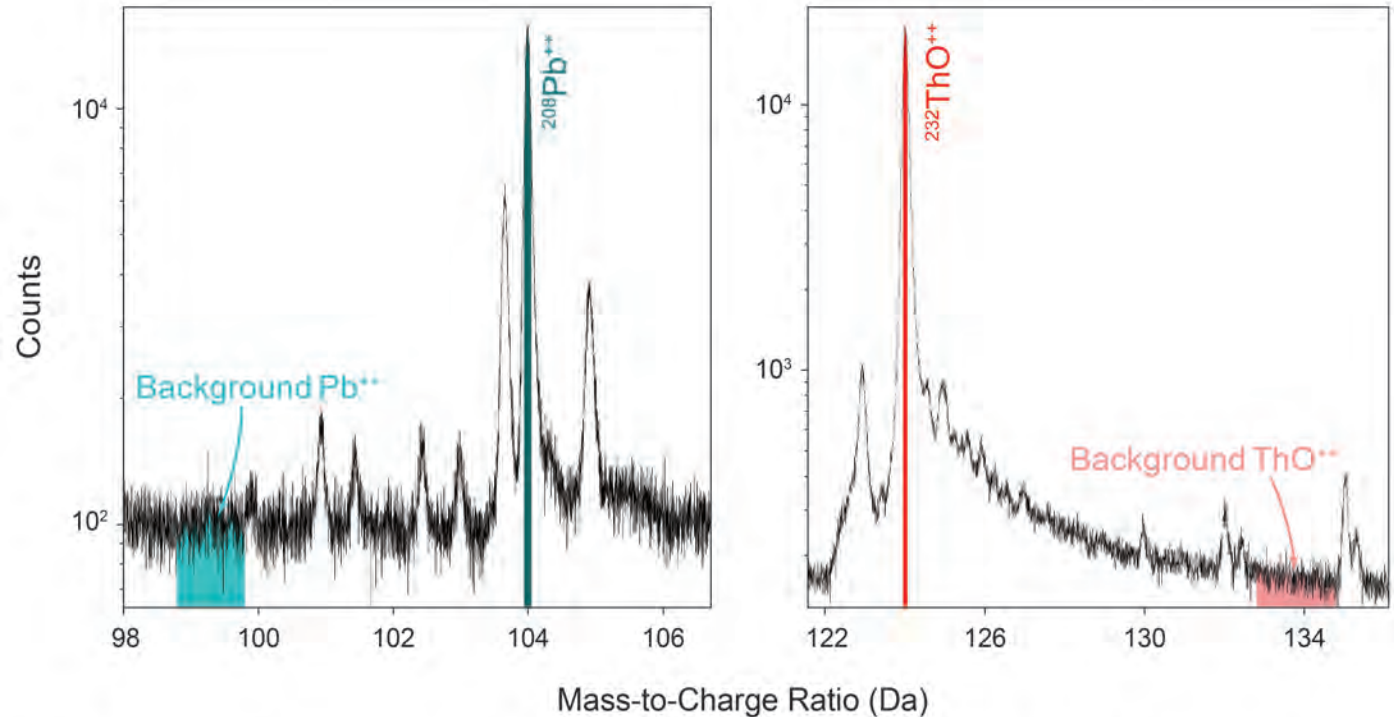


Figure S1: APT Mass-to-charge spectra of monazite showing the local region to $^{208}\text{Pb}^{++}$ and $^{232}\text{ThO}^{++}$ for background estimation.